

RESEARCH ARTICLE

10.1029/2019JB017614

Key Points:

- An updated tectonic velocity solution for the southeastern margin of the Tibetan Plateau
- Block kinematic model constrained by GNSS data and an Euler pole clustering algorithm resolves the new Daliangshan-Yingjing-Mabian block
- Both the continuum and the microplate deformation patterns are present in the southeastern margin of the Tibetan Plateau

Supporting Information:

- Supporting Information S1
- Data Set S1

Correspondence to:

X. Rui,
xurui_3@163.com

Citation:

Rui, X., & Stamps, D. S. (2019). Strain accommodation in the Daliangshan Mountain area, southeastern margin of the Tibetan Plateau. *Journal of Geophysical Research: Solid Earth*, 124. <https://doi.org/10.1029/2019JB017614>

Received 28 FEB 2019

Accepted 24 AUG 2019

Accepted article online 29 AUG 2019

Strain Accommodation in the Daliangshan Mountain Area, Southeastern Margin of the Tibetan Plateau

X. Rui¹  and D. S. Stamps² 

¹Research Institute of Disaster Reduction and Emergency Rescue, Sichuan Earthquake Agency, Chengdu, China,

²Department of Geosciences, Geodesy and Tectonophysics Laboratory, Virginia Tech, Blacksburg, VA, USA

Abstract The Xianshuihe-Xiaojiang fault system (XXFS) plays a crucial role in accommodating relative motions of the south China block and the expanding Tibetan Plateau. Compared to the narrow southern and northern segments of the XXFS, the central section (also referred to as the Daliangshan mountain area) is broader and dissected by a network of faults. Geologic studies suggest that three major NNW trending faults may dominate slip partitioning of more recent faults in this region. However, due to accessibility issues, sparse geodetic studies have constrained geodetic fault slip rates with contradictory results. In this study, we use 17 new Global Navigation Satellite System sites combined with existing solutions to investigate slip partitioning of the region. We derive a tectonic velocity solution, develop a block kinematic model constrained by Euler pole clustering technique, and calculate geodetic fault slip rates to compare with geologic fault slip rates. We confirm that the Anninghe-Daliangshan sliver (ADS) is a distinct, rigid block, and we resolve a new, rigid Daliangshan-Yingjing-Mabian block (DYB). Kinematic modeling predicts long-term slip rates that suggest both the ADS and the DYB partition (~10.0–12.0 mm/year) relative motion between the Tibetan Plateau and south China block in the central XXFS, reconciling geologic observations. We suggest that both the continuum and microplate deformation patterns are present in our study area, of which the local tectonics is better explained by the microplate model, but scale of the kinematics makes its motion more consistent with the continuum model.

1. Introduction

The southeastern margin of the Tibetan Plateau is segmented by the 1,200-km-long Xianshuihe-Xiaojiang fault system (XXFS) that separates the Tibetan plateau from the South China block (Figure 1). Two end-member models have been proposed for deformation mechanism of the Tibetan Plateau. In one view (hereafter called “the microplate model”), the India-Eurasia collisional deformation (crustal shortening) is suggested to be absorbed laterally along the large-scale narrow bounding fault zones through lithosphere extrusion (e.g., Leloup et al., 1995; Meade, 2007; Replumaz & Tapponnier, 2003; Shen et al., 2005; Tapponnier et al., 1982). Alternatively (hereafter called “the continuum model”), collisional stress is thought to be partitioned by numerous, isolated fault structures resulting in continuous deformation (e.g., Copley & McKenzie, 2007; England & Houseman, 1986; Houseman & McKenzie, 1982; Royden et al., 1997, 2008; Shen et al., 2001; Sternai et al., 2016). Understanding slip partitioning across the margin of the Plateau, for example, the XXFS, is crucial for unraveling how strain is accommodated and the corresponding mechanisms driving deformation at the surface.

The XXFS can be divided into three segments: the northern (Xianshuihe) and southern (Xiaojiang) fault segments, which are characteristically narrow (e.g., He et al., 2008; Zhang, 2013), and the central section (Figure 1). The central section of the XXFS, also referred to as the Daliangshan mountain area, is dissected by a network of NNW trending, left-lateral branching faults (e.g., Wang, 1998; Zhang, 2013), of which the Anninghe-Zemuhe, the Daliangshan, and the Yingjing-Mabian from west to east are thought to be the three major faults that dominate the slip partitioning of this region according to geologic studies (see below for more details). Here, we refer to the spindle-like tectonic area (Figure 1b) enclosed by the Anninghe-Zemuhe and the Daliangshan faults as the Anninghe-Daliangshan sliver (ADS) following Loveless and Meade (2011).

Previous studies suggest that the total left-lateral displacement on the XXFS (~60 km) remains approximately constant along most of its 1,200-km length (e.g., He et al., 2006, 2008; Wang, 1998; Zhang et al., 2013). In Table 1 we list long-term slip rate estimates based on geomorphologic observations, such as dating

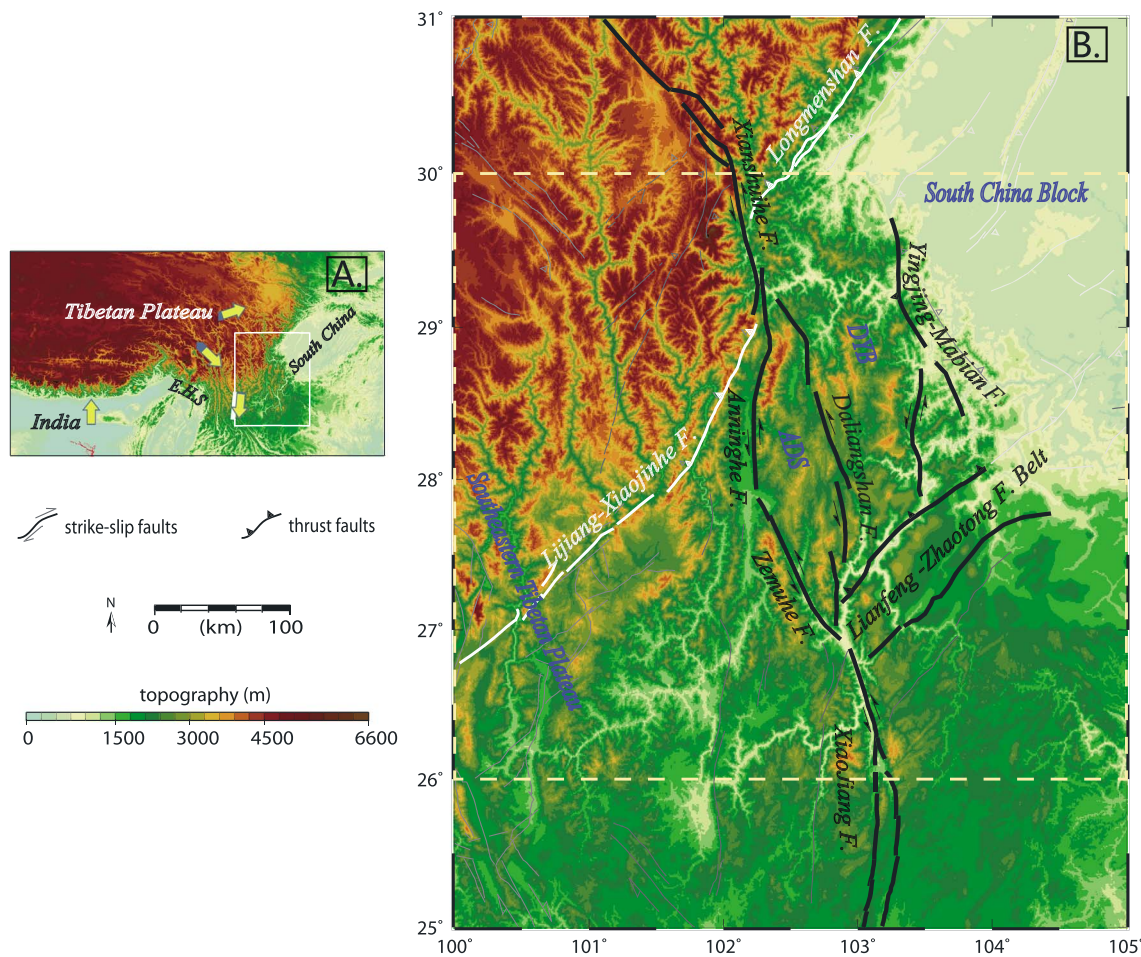


Figure 1. (a) The location of the southeastern margin of the Tibetan Plateau (white box) relative to the Tibetan Plateau and the South China block. EHS = the eastern Himalayan Syntaxis (see section 2). (b) Simplified map of the tectonic units used in this study. Black thick lines represent the fault strands related to the Xianshuihe-Xiaojiang fault system. Thick white lines represent the surrounding faults that are prominent in the study area. F. = Fault. The yellow dashed box shows the regional focus of this study. ADS = the Anninghe-Daliangshan sliver (see section 1); DYB = the Daliangshan-Yingjing-Mabian block (see section 4).

river/land offsets and trenching, and aerophotographic data along the northern (Xianshuihe) and southern (Xiaojiang) segments of the XXFS, as well as the Anninghe-Zemuhe faults. Available geological data of slip rates on these three faults (the Xianshuihe, the Xiaojiang, and the Anninghe-Zemuhe faults) are largely consistent at $\sim 12 \pm 3$ mm/year (Chen et al., 2000; Qian et al., 1990; Wen, 1993; Xu et al., 2003), $\sim 11 \pm 3$ mm/year (He et al., 2002; Jun et al., 2003; Zhang & Xie, 2001), and $\sim 6 \pm 2$ mm/year (Du, 2000; He et al., 1999; He & Yasutakyr, 2007; Qian, 1992; Ran et al., 2008; Xu et al., 2014), respectively. But geologic slip rate estimates are sparse along the Daliangshan fault and eastern Yingjing-Mabian fault sections of the central XXFS. The available geologic studies suggest that their slip rates are $\sim 4 \pm 1$ mm/year (He et al., 2008; Zhou et al., 2003) and 2 ± 1 mm/year (Xu et al., 2014; Zhang et al., 2005), respectively. Thus, the sum of the slip partitioned on the entire XXFS fault system would be balanced at the rate of $\sim 12 \pm 3$ mm/year.

Extensive Global Navigation Satellite System (GNSS) observations have been used to measure crustal motions along the northern and southern XXFS as well as the Anninghe-Zemuhe fault, but due to inaccessibility issues, corresponding estimates of the Daliangshan and Yingjing-Mabian fault are poorly constrained. As a result, several recent studies neglect the Daliangshan and Yingjing-Mabian faults when using GNSS data for plate kinematic modeling (e.g., He & Lu, 2007; Rui & Stamps, 2016; Wang et al., 2011; Zhang et al., 2013; Zheng et al., 2017) and also earthquake potential calculations (e.g., Jiang et al., 2015; Zhao et al., 2015). A few geodetic studies have taken these two faults into account, however. Table 1 lists geodetically estimated slip rates on the three key faults in the central XXFS from these studies. We note that for the first five geodetic studies in Table 1, the authors use nearly the same data set but derive significantly different

Table 1
Geodetic and Geologic Estimates of Fault Slip Rates (mm/year) of the XXFS

Sources	Anninghe F.	Zemuhe F.	Daliangshan F.	Yingjing-Mabian F.	Xianshuihe F. ^c	Xiaojiang F. ^c
Geodetic estimates of slip rates						
Shen et al. (2005) ^a	4 ± 2	7 ± 2	4 ± 2	N/A	~10.5 ± 2	7 ± 2
Wang et al. (2008)	5.1 ± 2.5	2.8 ± 2.3	7.1 ± 2.1	1.2 ± 1.2	~13	9.4 ± 1.2
Loveless and Meade (2011)	9.1 ± 1.1 –	N/A	1.7 ± 1.1 –	N/A	~11	10.5 ± 0.3
	10.0 ± 1.0		2.3 ± 1.1			
Cheng et al. (2011)	5.5 ± 0.8	6.7 ± 0.7	4.0 ± 0.8	N/A	11.3 ± 1.1	8.2 ± 1.1
Zhang (2012) ^b	~5	5.5 ± 1.5	2~3	<1	9.5 ± 1.5	N/A
Wang et al. (2017a)	6.2 ± 0.4	4.4 ± 0.7	6.0 ± 0.5	N/A	14.0 ± 0.6	12.7 ± 0.2
Geologic estimates of slip rates						
(1) Qian (1992); (2) Ran et al. (2008); (3) Xu et al. (2014); (4) He and Yasutaky (2007); (5) Du (1994); (6) Du (2000); (7) He et al. (1999); (8) Zhou et al. (2003); (9) He et al. (2008); (10) Zhang et al. (2005); (11) Xu et al. (2014); (12) Qian et al. (1990); (13) Wen (1993); (14) Chen et al. (2000); (15) Xu et al. (2003); (16) Zhang and Xie (2001); (17) He et al. (2002); (18) Jun et al. (2003)	~6 ± 2 (1,2,3,4)	~6 ± 2 (4,5,6,7)	~4 ± 1 (8,9)	~2 ± 1 (10,11)	~12 ± 3 (12,13,14,15)	~11 ± 3 (16,17,18)

Note. N/A = not applicable; XXFS = Xianshuihe-Xiaojiang fault system.

^aShen et al. (2005) first estimate the combined slip rate across the Anninghe and the Daliangshan faults and then allocate the slip rate on each fault by averaging.

^bZhang (2012) construct a velocity profile in an east-west direction across the Xiaojinhe, the Anninghe, the Daliangshan, and the Mabian faults (Figure 6 therein). However, because the profile is not normal to the Daliangshan Fault and the Mabian Fault, it is difficult to resolve the estimated slip rate on these faults.

^cFor Xianshuihe and Xiaojiang fault segments, several studies divide them into smaller segments. We take the average of the slip rate estimates for the multiple segments.

slip rates along the faults in the central XXFS due to data deficiency. The estimated geodetic slip rates on the Anninghe fault range from $\sim 4 \pm 2$ to 10 ± 1.0 mm/year (Loveless & Meade, 2011; Shen et al., 2005). The slip rate on the Zemuhe fault varies from 2.8 ± 2.3 to 7 ± 2 mm/year (Shen et al., 2005; Wang et al., 2008). And the slip rate on the Daliangshan fault varies from 1.7 ± 1.0 to 7.1 ± 2.1 mm/year (Loveless & Meade, 2011; Wang et al., 2008). Only two studies have explored geodetic slip rates on the Yingjing-Mabian fault (Wang et al., 2008; Zhang et al., 2013). Table 1 also lists the slip rate estimates from these studies on the northern XXFS (Xianshuihe) and the southern XXFS (Xiaojiang) fault segments. We note that a few studies (e.g., Cheng et al., 2011; Wang et al., 2008) divide these two faults further into smaller segments but show no significant slip rate differences. We therefore take the average of slip rate estimates along the multiple segments. The general agreement between the short-term (geodetic) and long-term (geological) slip rates on the Xianshuihe and the Xiaojiang faults suggests steady deformation rates on the northern and southern XXFS.

In this paper, we investigate conflicts among the geologically and the geodetically estimated slip rates in the central XXFS, which is crucial for understanding the mechanisms driving surface deformation in the southeastern margin of the Tibetan Plateau (e.g., the aforementioned two end-member models). To do so, we develop a new tectonic velocity solution that constrains a kinematic block model of the region and define the present-day fault slip rates. Blocks are delineated using an Euler pole clustering algorithm developed by Savage (2018), which allows us to characterize the extent and rigidity of the tectonic units in this region. We confirm that the Anninghe-Daliangshan sliver (ADS) is a distinct, rigid block, and we resolve a new, rigid Daliangshan-Yingjing-Mabian block (DYB) to the east bounded by the Yingjing-Mabian fault. We find that the data west of ADS can only be fit by considering a permanent strain rate.

2. Tectonic Setting

Figure 1b shows a simplified map of the major tectonic units around the southeastern margin of the Tibetan Plateau (e.g., Loveless & Meade, 2011; Shen et al., 2005; Wen et al., 2013; Zhang, 2013).

The ongoing postcollisional convergence between the Indian and Eurasian plates since ~ 50 Ma ago has caused 2,000 to 2,500 km of crustal shortening (e.g., England & Houseman, 1986; Harrison et al., 1992; Wang, 1998). Such shortening is mainly absorbed by the large-scale thrusting of continental lithosphere, bulk deformation, and lateral extrusion of the Eurasian lithosphere (e.g., Houseman & McKenzie, 1982;

Royden et al., 2008; Tapponnier et al., 1982; Thatcher, 2009). While thrusting and topographic growth of the southern Tibet occurs, large fragments of the Eurasian lithosphere were extruded eastward and south-eastward out of the collision zone (Figure 1a, yellow arrows). Southeastward extrusion, together with the combined effect of surrounding forces, for example, slab rollback along the Sunda and trench retreat of the Pacific oceanic subduction zone (e.g., Guzman-Speziale, 1996; Royden et al., 2008; Shen et al., 2001; Sternai et al., 2016), drives the southeastern Tibetan Plateau to rotate fast around a pole near the eastern Himalayan Syntaxis (Figure 1a). In the meanwhile, due to resistance of the cratonic south China block to the east, fast surface motions of the southeastern Tibetan Plateau are greatly impeded along their boundary region (where the XXFS is located, Figure 1b), leading to distinct strain accumulation, stress partitioning, and seismic activities (see Figure S1 in the supporting information for representative focal mechanisms of seismic events in this region). As described in section 1, the microplate model and the continuum model have been proposed to explain the deformation mechanism (e.g., strain partitioning) of the Tibetan Plateau. The microplate model emphasizes that the tectonic stresses are maintained by a limited number of large-scale elastic-plastic tectonic blocks in the upper lithosphere. The continuum model, however, suggests that the tectonic stresses are predominantly maintained by the weaker, ductile lower crust and/or mantle lithosphere beneath the rigid upper crust. In this model, the lithosphere is thought to be deformed pervasively (e.g., Copley & McKenzie, 2007; England & Houseman, 1986; Houseman & McKenzie, 1982; Royden et al., 1997; Royden et al., 2008; Shen et al., 2001; Sternai et al., 2016). The distinction between the two models becomes ambiguous as block size decreases and the number of faults increases (Thatcher, 2009).

Historically, the XXFS has been responsible for at least 14 $M > 7.0$ earthquakes recorded since 814 (e.g., Allen et al., 1991; Deng et al., 2003; Han, 2004; Shen et al., 2005; Wang, 1998; Zhang et al., 2013). The northern, strike-slip XXFS (Xianshuihe fault), trending N40–50°W, has produced at least eight earthquakes with magnitude $\geq M 7$ along its 350-km-length since 1725 (e.g., Allen et al., 1991). The southern end of the Xianshuihe fault bifurcates into two strands. One strand connects to the south trending Anninghe Fault and the other to the Daliangshan fault (Figure 1b). To the south, the NNW trending, 400-km long, Xiaojiang Fault (southern XXFS) has produced more than 10 earthquakes of $\geq M 6$ since 1500 (He et al., 2002; Jun et al., 2003).

The central XXFS, which is the main focus of this study, is located around the Daliangshan mountain area, which is bounded on the west by the Longmenshan and Anninghe-Zemuhe faults and on the east by the Yingjing-Mabian and Lianfeng-Zhaotong faults. Since being sandwiched by the expanding southeastern Tibetan Plateau and the stable south China craton, the relative Tibetan Plateau-south China block motion has been dramatically accommodated by this region resulting in extensive tectonic deformation and numerous devastating earthquakes (e.g., Zhang et al., 2013). At least three $M > 7$ earthquakes were recorded historically along the Anninghe-Zemuhe fault, of which two (1480 Yuexi $M 7.5$ earthquake and 1536 Luguzhou $M 7.5$ earthquake) are on the Anninghe fault and one (1850 Xichang $M 7.5$ earthquake) on the Zemuhe fault (e.g., Sun et al., 2010; Wang et al., 2017b). Because of long seismic gaps, the Anninghe fault has been considered to have the potential for a large earthquake of $\sim M 7.5$ since the end of last century, while the Zemuhe fault shows lower seismic potential (e.g., Kuwahara et al., 2012; Wen et al., 2008). Historical earthquake records along the Daliangshan fault show that no destructive earthquakes have occurred, but three $M > 5$ events have ruptured the fault. Nonetheless, Song et al. (2002) attribute the missing records of $M > 7$ earthquakes on the Daliangshan fault to its remote and inaccessible location. Using the trenching technique, Song et al. (2002) and He et al. (2008) suggest that at least nine $M > 7$ paleo-earthquakes have occurred along this fault, indicating that the seismicity along the Daliangshan fault zone is as pronounced as that of the other fault zones in the XXFS.

The arc-like XXFS is narrow along the Xianshuihe fault and along the Xiaojiang Fault, both trending approximately NNW. But the Anninghe-Zemuhe fault in the central XXFS forms a reverse arc. He et al. (2008) suggest that the arcuate Daliangshan fault zone is younger and may be replacing strain accommodation on the Anninghe-Zemuhe fault such that the Anninghe-Zemuhe fault could become inactive.

The easternmost ~250-km long Yingjing-Mabian fault has been active since Late Quaternary (Tang & Han, 1993) and bounds the southwestern margin of the Sichuan basin (Figure 1b). There is a pronounced elevation change across the Yingjing-Mabian fault, similar to the Longmenshan fault (Figure 1) where the

unexpected 2008 M8.0 earthquake occurred. Compared to the Daliangshan fault, the Yingjing-Mabian fault is more seismically active. At least five $M > 6.5$ earthquakes, of which two are $>M7$ (Cheng et al., 2014), were recorded since 1216 (Yi et al., 2010), suggesting that the Yingjing-Mabian fault warrants special attention by the broader community.

Figure 1b also portrays the Lianfeng-Zhaotong fault belt positioned at the southernmost end of the Daliangshan mountain area. It is responsible for the latest 2014 Ludian Mw 6.1 earthquake. Geologic studies suggest that the Lianfeng-Zhaotong fault belt is part of the boundary of the South China block (e.g., Wen et al., 2013; Zhang et al., 2003) and is connected to the west with the XXFS. As the Lianfeng-Zhaotong fault belt is nearly perpendicular to the Anninghe-Zemuhe fault, the Daliangshan fault, and the Yingjing-Mabian fault, it plays an important role in accommodating the southeastward motion of the central XXFS resulting from the southeastward movements of the Tibetan Plateau (e.g., Wen et al., 2013).

In addition to the aforementioned active faults, the Longmenshan and the Lijiang-Xiaojinhe faults are two other prominent fault features sitting around the XXFS (Figure 1b, white curves). The northeast trending Longmenshan Fault is a prominent topographic feature in the Sichuan province that separates the cratonic Sichuan Basin and the eastern margin of the elevated Tibetan Plateau. Average geologic slip rates along the Longmenshan Fault, for the past ~10,000 years, have been estimated to be slow at ~1 mm/year based on trenching and satellite imagery investigations (e.g., Densmore et al., 2007; Zhang et al., 2013), consistent with geodetic estimates (e.g., King et al., 1997) before the unexpected 2008 Wenchuan Mw7.9 earthquake. As suggested by Xiang et al. (2002), the Lijiang-Xiaojinhe fault is a major transverse fault that accommodates southeastward extrusion of the Tibetan Plateau based on geologic and seismic investigations. However, geodetic studies do not support this notion (e.g., Qiao et al., 2004). Field investigations and satellite imagery reveal its geologic slip rate of ~1–3 mm/year (Xiang et al., 2002; Zhang, 2013).

In this work, we mainly focus on the central section of the XXFS, which is shown as a dashed box in Figure 1b.

3. GNSS Data Analysis

The GNSS data we process are mainly from four sources: (1) The Crustal Movement Observation Network of China (CMONOC), operated by the China Earthquake Administration. The CMONOC network contains 79 campaign GNSS sites and 9 continuous GNSS sites (SCJL, SCLT, SCMN, SCNN, SCPZ, SCSM, SCXD, SCYX, and SCYY) in our study area. Observation epochs date back to as early as 1999. (2) The Sichuan GNSS Network of the Sichuan Earthquake Agency, which contains 17 continuous GNSS sites in the region (GANL, HANY, KAIY, GYAO, XICH, LIUH, ZHUH, BIER, SIGQ, ZHJI, LUOH, MABI, JUNL, YBIN, MOXI, LESH, and ROXI). Some observations date back to early as 2006. (3) The GNSS sites operated by the Sichuan Surveying and Mapping Bureau. This network contains one continuous GNSS sites (PZHA), which was collected since 2012. (4) The pre-2008 velocity solution from Zhang (2013). It contains the velocity information of most of the sites installed before 2008 by different research institutes, of which the raw data are not accessible, but their velocity solutions are broadly used by the community (e.g., Cheng et al., 2011; Shen et al., 2005; Wang et al., 2008; listed in Table 1).

We processed the GNSS data loosely following the procedures described in McClusky et al. (2000), McCaffrey et al. (2007), and Rui and Stamps (2016) using the GAMIT-GLOBK GNSS processing software (Herring et al., 2016). We combine the phase observations from the GNSS receivers with observations from 5 to 10 continuous IGS stations to estimate loosely constrained positions, atmospheric parameters, and Earth orientation parameters, each with associated covariance matrices. We then combine these estimates and their covariances as “quasi-observations” (Dong et al., 1998) with the estimates and covariances from the Massachusetts Institute of Technology (MIT) global analysis to estimate positions at each epoch. Then, for continuous sites, we aggregate the daily estimates over periods of 7 days to reduce computational burden and better assess the long-term statistics of the positions following McCaffrey et al. (2007). For the campaign sites we use the daily estimate. We combine the position estimates into a cumulative solution to derive site velocities for the episodic and continuous sites separately, and then rotate and translate the two solutions into the Eurasian fixed 2008 International Terrestrial Reference Frame (Altamimi et al., 2012) with 58 common IGS sites evenly distributed around the world.

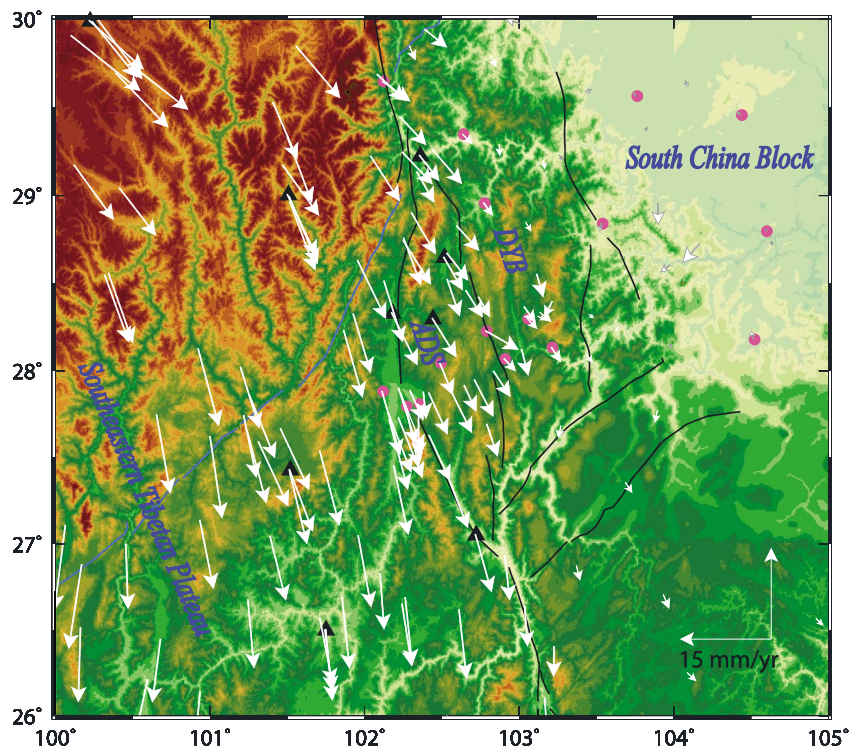


Figure 2. The updated interseismic GNSS velocity field with respect to the South China block. The labelled tectonic units are the same as that of Figure 1a. The pink circles are 17 continuous GNSS sites deployed by Sichuan Earthquake Agency and the black triangles are nine continuous GNSS sites deployed by CMONOC. For clarity, velocity uncertainties (please refer to Dataset S1) and fault names are not shown here. ADS = the Anninghe-Daliangshan sliver; DYS = the Daliangshan-Yingjing-Mabian block; GNSS = Global Navigation Satellite System; CMONOC = Crustal Movement Observation Network of China.

Realistic uncertainties for the estimated positions coordinates and velocities are obtained by adding both white and correlated noise to the phase observations and daily quasi-observations. To do so, we first assign 10 mm for the a priori phase error to make coordinate uncertainties approximately realistic with 2-min sampling following Herring et al. (2010). Second, we remove apparent outliers and downweight the daily observations for stations and time periods that reflect a higher than average scatter. Third, we add a random walk component to all continuous stations that we determined using the first-order Gauss-Markov algorithm (Herring, 2003; Reilinger et al., 2006). Finally, we add an estimate for random walk noise to the campaign data based on the average of that of the continuous stations and then recalculated the velocity solutions.

We then align the velocities of Zhang (2013) to our velocity framework by minimizing the residual velocities of seven common sites (DLHA, DXIN, LHAZ, WHJF, WUHN, XIAG, and XNIN). After transformation, the maximum differences at these fundamental/common sites are -1.11 and -0.72 mm/year in east and north direction respectively, comparable to their 1-sigma uncertainties.

Our final velocity field consists of 142 sites, of which 104 are from data source 1 to 3 and 38 are from Zhang (2013). The full velocity solution with respect to South China block (91.44°E , -13.36°N , $-0.0877^{\circ}/\text{Ma}$; see section 5) is provided in the supporting information in GLOBK velocity format (Data Set S1), shown in Figure 2, and made available through the UNAVCO repository.

4. Block Definition Using the Euler Pole Clustering Technique

We use the Euler pole clustering technique to automatically identify the first-order block geometries in this region and then use the *F* test based on block kinematic models to measure their statistical significance.

The Euler pole clustering technique applied to plate tectonics was first introduced by Savage and Simpson (2013) and updated by Savage (2018). The method automatically (without any apriori input of tectonic

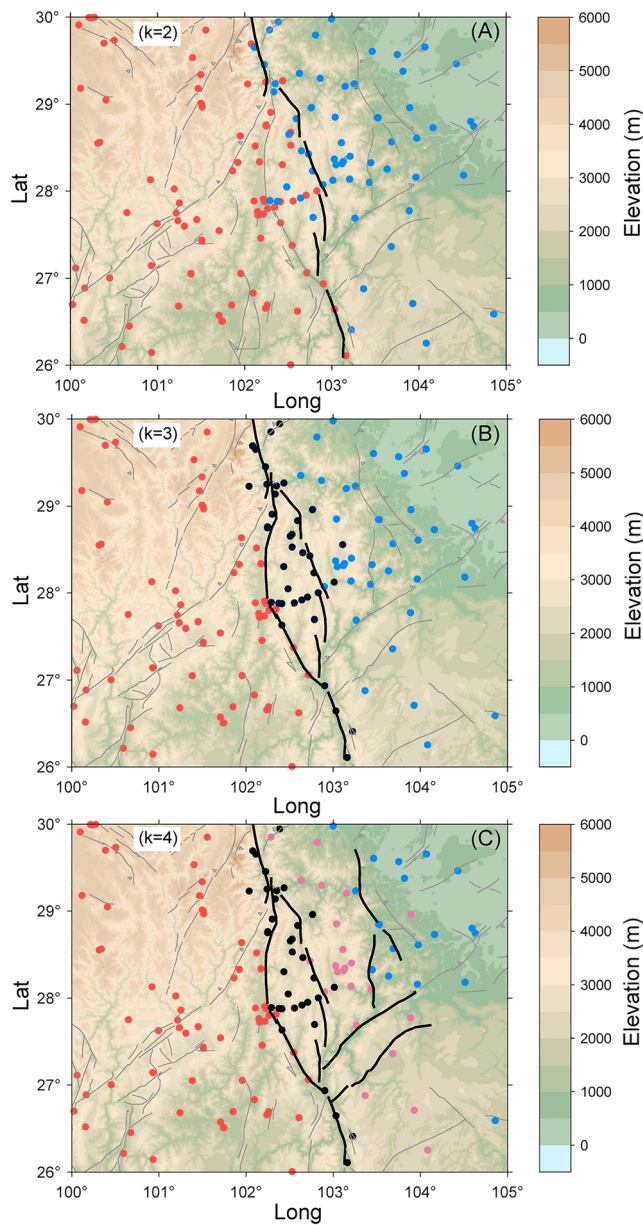


Figure 3. The assignment of Global Navigation Satellite System (GNSS) stations to clusters based on the Euler vector clustering algorithm developed by Savage (2018). Each color corresponds to an individual cluster. Each plot is labeled by the value of k , the number of clusters.

information) assigns GNSS velocities to clusters (blocks) such that all stations in a cluster have approximately the same Euler vector. In this work, we follow the Euler pole clustering algorithm detailed by Savage (2018) to characterize the extent and rigidity of deformation units in this region based on the GNSS velocity vectors derived in section 3.

The discerned clusters (blocks) for $k = 2$ to 4 (k represents the number of clusters) are shown in Figure 3. We chose a maximum of $k = 4$ because the GNSS stations become randomly distributed and no physical boundaries can be easily discerned between the clusters with $k > 4$.

For $k = 2$ (Figure 3a), the study area is divided into two clusters (red and blue circles) approximately along the XXFS. We note that in the central XXFS, the physical boundary between the two clusters is unclear, indicating that a transition zone or more blocks may exist.

For $k = 3$ (Figure 3b), ADS emerges, suggesting its existence based on GNSS data between the Tibetan Plateau and the South China block.

For $k = 4$ (Figure 3c), a new cluster (magenta) is resolved east of the ADS, which we name the Daliangshan-Yingjing-Mabian block. This cluster is nearly parallel to the ADS (black dots) and is bounded to the east by the Yingjing-Mabian fault zone. The cluster further extends to the southernmost region of the study area beyond the Lianfeng-Zhaotong fault zone. However, considering (1) the prominence of the Lianfeng-Zhaotong fault zone detailed in section 2 (it bounds the southwestern margin of the Sichuan basin and intersects perpendicularly with the Daliangshan and the Yingjing-Mabian fault) and (2) the region south of the Lianfeng-Zhaotong fault zone has very sparse data (four sites) and two of them (H396, F357) have significantly large uncertainties (>2 mm/year for each horizontal component, see Data Set S1), we therefore remove these four sites and define the Lianfeng-Zhaotong fault zone as the southernmost boundary of the newly resolved block.

5. Block Kinematic Modeling

5.1. Statistical Significance of Resolved Blocks

To determine if the blocks resolved with the Euler pole clustering algorithm are significant, we test a series of block kinematic models that have freely slipping block boundaries using TDEFNODE (McCaffrey et al., 2007). We start with a one-block model (SC) and then iteratively add the CD, ADS, and DYB blocks. We use the F test (e.g., Stein & Gordon, 1984) to determine if the model is significantly improved by adding the CD, ADS, and DYB blocks:

$$F = \frac{(\chi_1^2 - \chi_2^2)/(p_1 - p_2)}{\chi_2^2/p_2} \quad (1)$$

where p_1 and p_2 denote the degrees of freedom of the two models. The χ^2 is defined as (e.g., Gordon et al., 1987):

$$\chi_N^2 = \sum_{i=1}^N \left(\frac{d_i^{\text{obs}} - d_i^{\text{pred}}}{\sigma_i} \right)^2 \quad (2)$$

where d_i^{pred} and d_i^{obs} are the predicted and observed velocity components, σ_i is the observed standard error of the corresponding velocity component, and N is the number of observations.

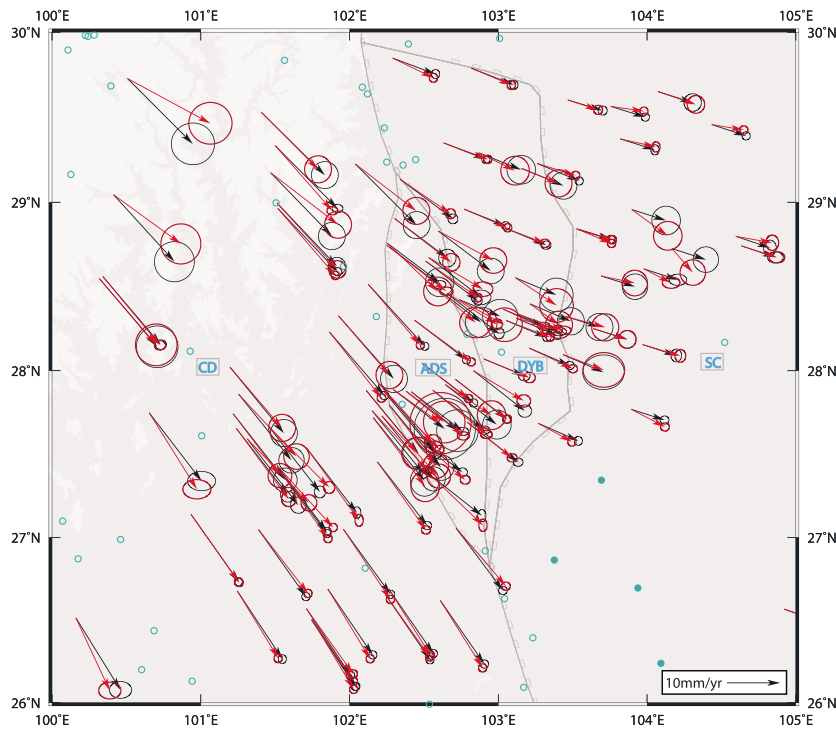


Figure 4. Observed (red vectors) and predicted (black vectors) velocities from the best fit model in a Eurasia reference frame. Green solid circles are 4 deleted sites described in section 4. Green open circles are deleted sites based on F described in section 5.1.

In this study, we use the 99% confidence level of the F test to reject the null hypothesis, and we use value of the reduced chi-squared, χ^2_v , defined as the ratio of χ^2 to the number of degree of freedom, as an indicator of good fit between the model and the data.

We use all GNSS vectors derived in section 3 (with the four sites described in section 4 removed) to perform the F test to check if the candidate blocks (CD, ADS, and DYB) can significantly improve the model fit at the 99% confidence level. F test results show that adding the CD, ADS, and DYB subblocks significantly improve the model fit with 100.00%, 100.00%, and 100.00% confidence levels, respectively, indicating that these blocks are warranted under the 99% confidence level. F test results also show that adding the Lijiang-Xiaojinhe fault (see Figure 1b and section 2) to divide the CD into two subblocks does not improve the model fit significantly at the 99% confidence level.

We then include the four resolved subblocks into our block model and calculate their angular velocity vectors, modeled velocities, and corresponding velocity residuals. We remove the velocities with SNR (signal-to-noise ratio of velocity residual to velocity uncertainty) larger than 2.5 loosely following Shen et al. (2005) to detect possible outliers caused by monument instability, localized deformation, transient signals, and so forth. Then, we rerun TDEFNODE. We iterate this step until no velocity residuals have SNR larger than 2.5. Figure 4 shows the 31 deleted sites after iteration (green open circles) and the four deleted sites described in section 4 (green solid circles). We note that many of the deleted sites are located closely to the clustered fault traces (see Figure S2 for relative position between the deleted sites and all active fault traces in this region), indicating that motions of these sites are likely affected by elastic strain accumulation of the faults or unrecognized smaller blocks. Since majority of them are far away from the Daliangshan mountain area and are discarded from the final kinematic model, we do not need to concern them too much.

With the reduced GPS velocity data, we recalculate the F test for each candidate subblock. The results confirm that adding the CD, ADS, and DYB subblocks significantly improves the model fit with 100.00%, 100.00%, and 100.00% confidence levels, respectively, but adding the Lijiang-Xiaojinhe fault improves the model fit with less than 99% confidence level (56.39%). The F tests also indicate that adding permanent

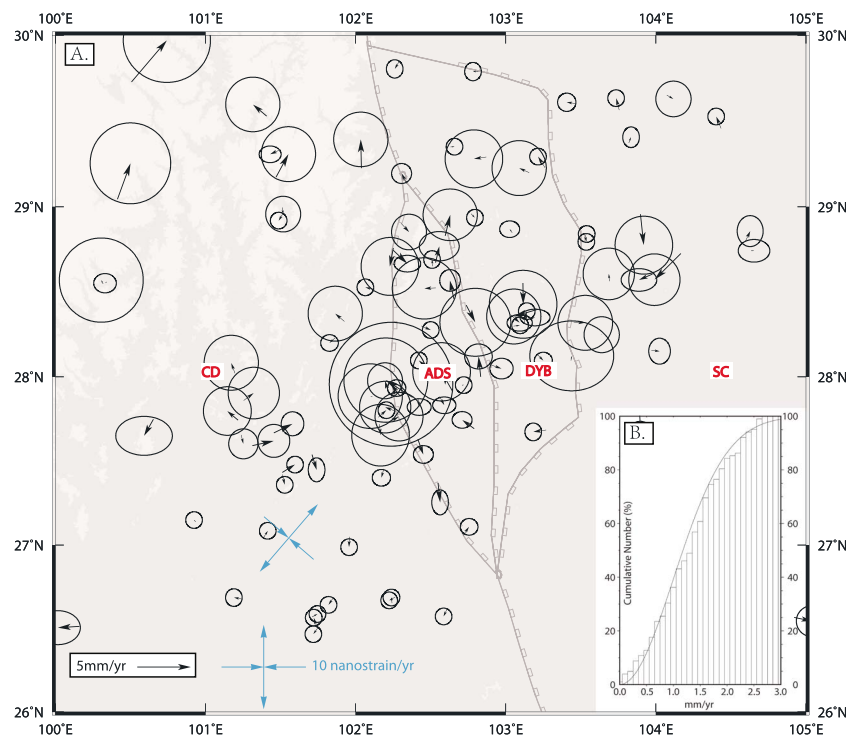


Figure 5. (a) Permanent strain rate (nonrecoverable) in block CD and velocity residuals of the best fit model with 68% uncertainty ellipses (one standard deviation). (b) Cumulative histogram of signal-to-noise ratios of the velocity residuals (bins) compared with a (2-D) theoretical chi-squared distribution (curved line) expected from assuming that the north and east residuals are normally distributed with unit variance.

strain rate (the uniform, nonrecoverable strain rate within the block; McCaffrey, 2005; McCaffrey et al., 2007) to CD, ADS, and DYP, respectively, improves the model fit with probabilities of 100.0%, 83.23%, and 9.34%. These results suggest that all blocks, but CD, deform rigidly. The permanent strain rate is derived from the residual of observed velocity relative to the velocity predicted by the Euler vector, and such velocity residual may arise from various sources, including (1) unrecognized smaller block(s), localized transient motion or elastic-plastic rheology, (2) unrealistic assumption that faults slip freely along the block boundaries or not all GNSS sites within the strain accumulation zone (e.g., within ~30 km of faults) have been excluded from model. If so, unmolded elastic strain along the block boundaries may contaminate the rigid-body motion, and (3) framework alignment issue may exist while incorporating our new velocity solution with the Shen et al. (2005) tectonic velocity solution. The combined solution uncertainties should be kept in mind because of framework alignment issues, which may cause data incompatibility and artificial distortion (deformation) within the block. We note that the pattern (e.g., the direction of compressional and extensional components) of estimated permanent strain rate in block CD (Figure 5) is consistent with strain rate pattern estimated by interseismic GNSS velocity (e.g., Figure 7e of Kreemer et al., 2014) and strain pattern estimated by the focal mechanism of historical earthquakes (e.g., Figure 5b of Xu et al., 2016). Such consistency should exclude the framework alignment issue. The velocity residuals along the block boundaries are quite small without an estimate permanent strain rate in block CD (Figure S3), indicating that the free slip or strain accumulation issue can be excluded. Therefore, we propose that permanent strain rate within CD arises from unrecognized smaller block(s), localized transient motion, or elastic-plastic rheology. Please note that the permanent strain rate signal (estimated by velocity residuals that are at the level of 1–2 mm/year in CD; Figure S3) is about 1 order smaller than the region's background tectonic motion (at the level of ~10 mm/year, e.g., Figure 5).

Statistically, our results indicate a good fit between the data and model. Our preferred model has a reduced chi-squared $\chi^2_v = 1.35$. The normalized root-mean-square values are 1.18 mm/year on average, with an uncertainty range of ± 0.1 mm/year. The weighted root-mean-square values are 0.80 mm/year on average,

Table 2*Statistics and Euler Poles for Best Fit Model in a Eurasia Reference Frame*

Block	N	NRMS	WRMS	Longitude	Latitude	Omega	Sig omega	Maximum	Minimum	Azimuth
SC	36	1.063	0.738	91.44	-13.36	-0.087	0.077	56.84	1.36	195.82
DYB	38	1.013	0.639	91.78	-0.05	-0.148	0.091	28.50	0.70	199.44
ADS	42	1.319	0.908	78.00	-7.14	-0.164	0.115	46.35	0.66	212.79
CD	88	1.074	0.714	62.20	-6.41	-0.178	0.041	22.39	0.50	226.89

Note. N is the number of data in the block, twice the number of vectors for GNSS data; Latitude, Longitude, and Omega give the location and rotation rate ($^{\circ}/\text{Ma}$) of Euler pole for the block rotation relative to Eurasia reference frame, Sig omega is the uncertainty of the rotation rate ($^{\circ}/\text{Ma}$), and Maximum, Minimum, and Azimuth are the 68% confidence error ellipse (maximum/minimum axis and azimuth of maximum axis) for block rotation. NRMS = normalized root-mean-square; WRMS = weighted root-mean-square.

with an uncertainty range of $\pm 0.2 \text{ mm/year}$ for individual blocks. Detailed statistics and Euler poles from the best fit model are listed in Table 2.

5.2. Modeling Results

Observed (red arrows) and predicted (black arrows) velocities from the best fit model in a Eurasia reference frame are shown in Figure 4. Velocity residuals are shown in Figure 5, of which 75.5% (154 out of 204 observations) of velocity residuals fall between $\pm 1 \text{ mm/year}$ and 87.8% (179 out of 204 observations) of velocity residuals fall between $\pm 1.5 \text{ mm/year}$. Figure 5b compares the cumulative histogram of signal-to-noise ratios of the velocity residuals with a (2-D) theoretical chi-square distribution (curved line) expected from assuming that the north and east residuals are normally distributed with unit variance (e.g., McCaffrey et al., 2007). We find that our noise model matches the expected distribution of normalized residuals well except with some minor misfit: The excess of values to the left of the curve between 0%–25% and 95%–100% indicates that some of the uncertainties are too large (thus the number of small SNR observations are in excess of the theoretical value); the deficiency of values to the right of the curve between 40% and 90% indicates the removal of too many outliers (thus decreases the number of observations with large SNR).

Predicted long-term slip rates for our preferred model along the block boundaries are shown in Figure 6a. This figure illustrates that the Daliangshan fault, Anninghe-Zemuhe fault, and Yingjing-Mabian fault are slipping at the rate of 4.0–5.0, 4.0–5.0, and 1.0–2.0 mm/year respectively, warranting the prominent role of the Daliangshan fault in partitioning the SC-CD relative motion. The summation of these three slip rates shares the similar magnitude with that of the northward Xianshuihe fault (~9–10 mm/year) and the southward Xiaojiang fault (~9–11 mm/year), suggesting that slip partitioning along the entire Xianshuihe-Xiaojiang fault system is balanced, consistent with the geologic estimates (see section 2). In addition, we show the decomposed fault parallel and fault normal components of model predicted slip rates along the block boundaries in Figures 6b and 6c respectively. For more discussion, please refer to section 6.1.

6. Discussion

6.1. GPS Velocity Profile-Derived Slip Rates

To further verify predicted slip rates, we calculate fault slip rates by evaluating GNSS velocity profiles across fault strands defined in Figure 7. Because the focus of our study is the central XXFS, we only evaluate the velocity profiles across the faults located there. To calculate the velocity profile on each fault, we collect all GNSS velocities $\pm 200 \text{ km}$ across the fault, from west to east, with a profile swath of 100 km. For each profile, we decompose the collected GNSS velocities into two components, one is along the profile (fault normal, corresponding to the reverse slip information) and the other is perpendicular (fault parallel, corresponding to the strike-slip information) to the profile. Figure 8 shows the velocity profiles defined in Figure 7. In each subplot, we also project the location of adjacent fault strand (gray dotted curves) so that only sites located between the faults will be used for final slip rate estimate. The calculated fault parallel/normal slip rates are based on the difference of the center of each shaded region that is chosen and illustrated in Figure 8. The results are listed in Table 3.

In general, comparisons among Figures 6a (model predicted slip rate), 6b (decomposed fault parallel component of model predicted slip rate), and 6c (decomposed fault normal component of model

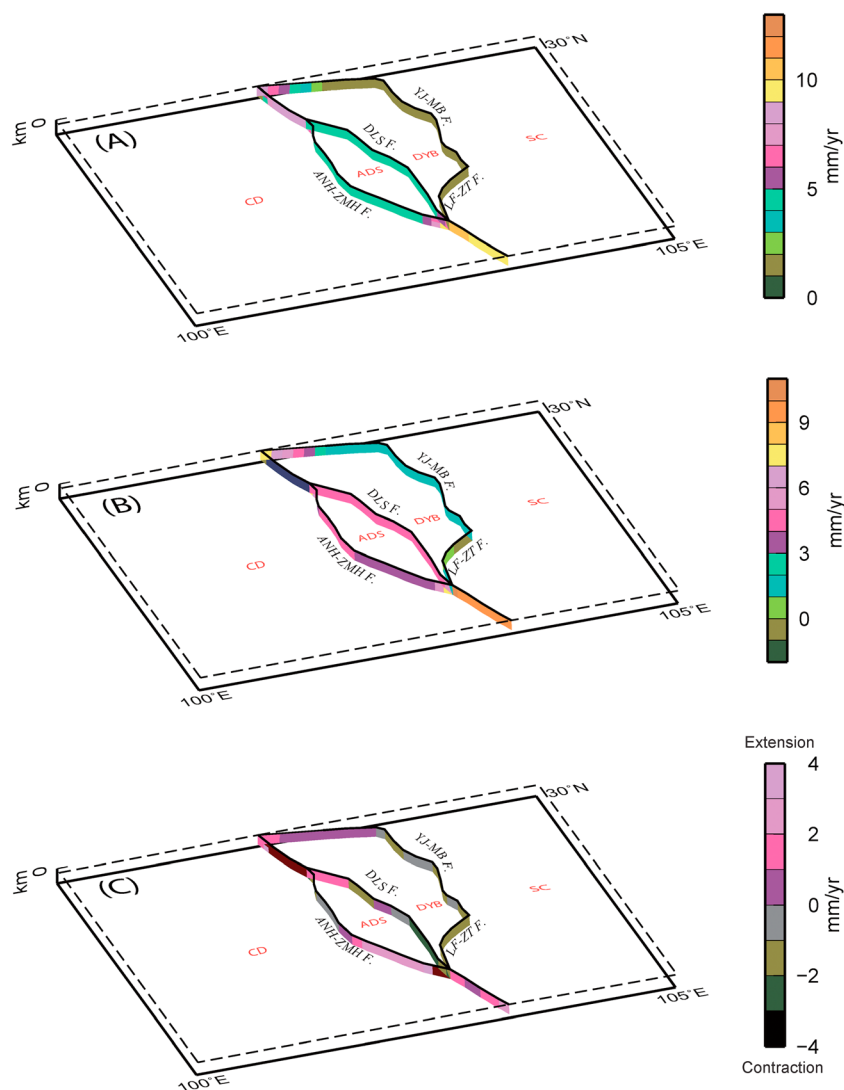


Figure 6. (a) Predicted slip rates of the best fit model. (b) Decomposed fault parallel component of the predicted slip rates. C. Decomposed fault normal component of the predicted slip rates. ANH-ZMH F. = Anninghe-Zemuhe Fault; DLS F. = Daliangshan Fault; YJ-MBF. = Yingjing-Mabian Fault; LF-ZT F. = Lianfeng-Zhaotong Fault.

predicted slip rate) and Table 3 (GNSS profile derived slip rate) show that the two types of slip rates agree well with each other. However, the velocity profile-derived slip rates provide more detailed information. Results listed in Table 3 indicate that first, overall, all faults but the Zemuhe fault contract. Second, for the Daliangshan fault zone from north to south, the magnitude of contraction rate appears to increase gradually. Third, for the Mabian fault from north to south, the strike-slip component decreases, while the contraction component increases. However, since such change is at the level of ~1 mm/year, more data are needed for confirmation. We note that the present-day crustal deformation around the Yingjing-Mabian fault zone shares similar surface motion patterns with the Longmenshan fault zone located immediately to the north where the unexpected 2008 Mw7.9 Wenchuan earthquake took place. That is, components of strike-slip and reverse are dominant for these two fault zones, and both of them share the large topographic gradient with the south China block (see section 2). Considering the disaster of the Wenchuan earthquake and high population in this region, we advise more efforts on infrastructure fortification against earthquakes and investments in earthquake monitoring for this specific region.

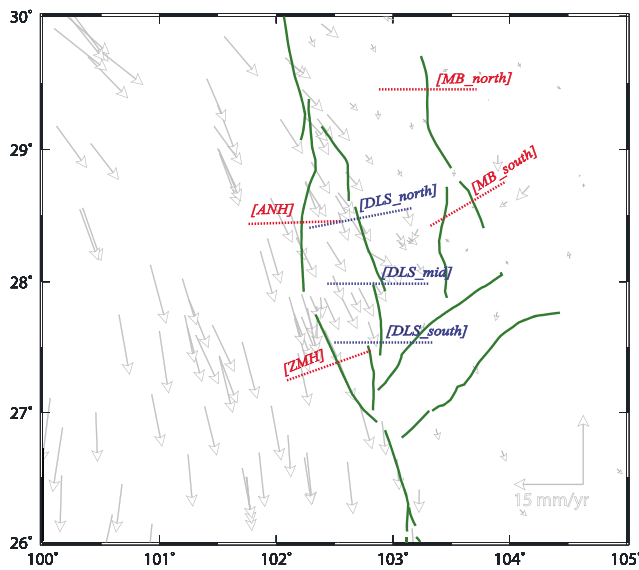


Figure 7. Position of velocity profiles used to calculate the fault normal and fault parallel velocity components shown in Figure 8. The gray arrows are the GNSS velocities also shown in Figure 2 in a South China block reference frame. For each profile, collect all the GNSS velocities ± 200 km across the fault, from west to east, with the profile swath of 100 km. MB = Mabian Fault; ANH = Anninghe Fault; DLS = Daliangshan Fault; ZMH = Zemuhe Fault.

slip exists and to what depth such aseismic slip may reach. Such uncertainty prevents us from precise evaluation of earthquake hazard (e.g., Bürgmann, 2000; Lyons et al., 2002); and (3) complicated interactions among spindle like fault network. Geodetic data must be dense enough (e.g., using GNSS and interferometric synthetic aperture radar data together) to distinguish the slip deficit between these closely adjacent fault segments (e.g., Chaussard et al., 2015).

6.3. Deformation Mechanisms

As described in section 1, two end-member models have been proposed to interpret the large-scale continental deformation between India and Eurasia. The first model, termed the microplate model, emphasizes that the tectonic stresses are maintained by a rigid, block-like upper crust. Because of the internal rigidity of the blocks, collisional deformation can only be accommodated laterally along the large-scale narrow bounding fault zones (e.g., Leloup et al., 1995; Meade, 2007; Tapponnier et al., 1982; Thatcher, 2007). The second model known as the continuum model suggests that the tectonic stresses are predominantly supported by a ductile lower crust beneath the rigid upper crust. In this model, the upper crust is thought to be driven and pervasively deformed by coupling to the viscous lower crustal flow resulting from gravitational spreading (e.g., Houseman & McKenzie, 1982; Royden et al., 1997). Which model best explains observations of surface deformation still remains controversial (e.g., Thatcher, 2009).

In this work, we evaluate the rigidity of CD, ADS, DYB, and SC blocks and find only that the data on the CD block are fit significantly better with a kinematic model that deforms internally. The other blocks in the region are rigid with strain accommodated by slip along their boundaries. These modeling results suggest both end-member models of deformation may be present in the southeastern margin of the Tibetan Plateau. On one hand, observations of surface kinematics in the CD block may provide evidence that ductile material beneath the brittle crust of the CD extrudes materials in the lower crust, which according to the continuum model, indicates gravitational spreading dominates part of the southeastern margin of the Tibetan Plateau. On the other hand, partitioning of tectonic stresses around rigid blocks occurs in the ADS and DYB (adjacent to the rigid SC), lending support to the microplate hypothesis. It is noteworthy that compared to the major blocks proposed by the microplate model, the block sizes of ADS and DYB, however, are very small ($\sim 200 \times 100$ km) such that it is difficult to consider deformation in this region to be completely plate like (e.g., Shen et al., 2005; Thatcher, 2009). Instead, as discussed in Thatcher (2009), when the block

6.2. Seismic Risk Implications for the Anninghe-Zemuhe Fault Zone

As mentioned in section 1, to evaluate the seismic hazards along the Anninghe-Zemuhe fault zone, some previous studies do not account for the influence of the Daliangshan and Yingjing-Maibian fault zones (e.g., Jiang et al., 2015; Zhao et al., 2015). Instead, they consider all of the GNSS sites east of the Anninghe-Zemuhe fault as belonging to the south China block (SC). However, as shown in Figure 6, both the Daliangshan and Yingjing-Maibian faults play significant roles in partitioning the CD-SC relative motion. Considering this region is in a high seismic potential (section 2), we suggest a new GNSS-based slip deficit model, and the following seismic risk model should be reevaluated by taking the Anninghe-Zemuhe, Daliangshan, and Yingjing-Maibian fault zones together into account.

Even though it is possible to calculate slip deficit rate on fault plane based on our GNSS data and reevaluate the earthquake hazard of this region, we decide to leave this research for follow-up work because of (1) lack of GNSS data within ~ 30 km of faults where frictional slip takes place. As shown in Figure 4, in the central section of XXFS, by removing small amount of GNSS sites (blue open circles) within ~ 30 km of faults, our free slip model fits GNSS data well, indicating that a very limited number of GNSS sites can constrain the nonfree (frictional) slip component of these faults; (2) uncertainty of existence of aseismic slip. Due to lack of geodetic/geological data, it is still not clear whether significant aseismic

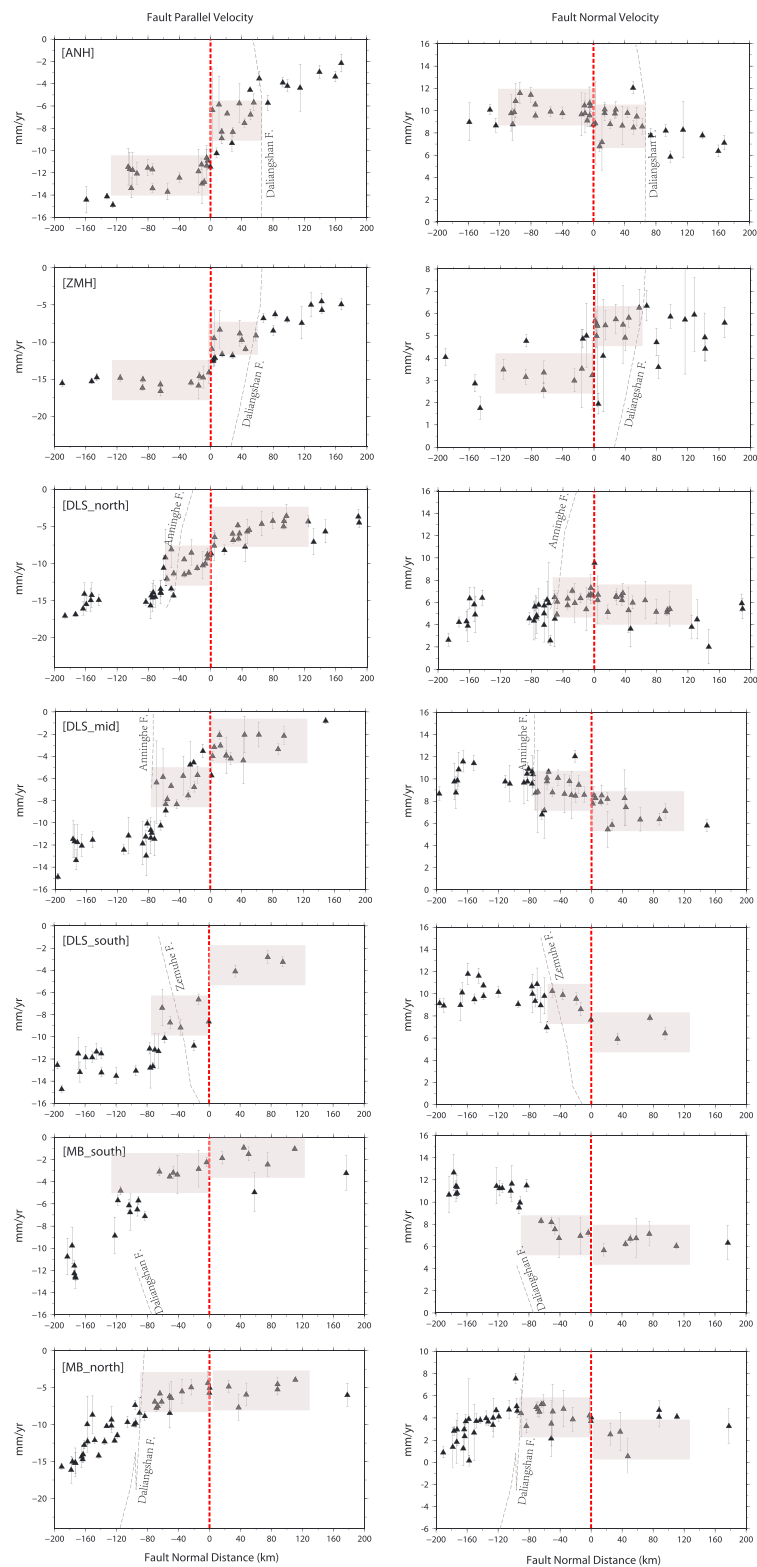


Figure 8. Global Navigation Satellite System (GNSS) velocity profile across fault strands as shown and labeled in Figure 7. Fault parallel (sinistral positive) and fault normal (extensional positive) components of slip rate are with respect to the distance along profile. The black triangles are GNSS sites located within the swath of corresponding profile. The red and gray dotted lines denote the position of the fault that we evaluate and the projection of the adjacent fault. Only data between these two faults are used for final slip rate estimate.

Table 3

Comparisons Between Model-Predicted and Global Navigation Satellite System (GNSS) Velocity Profiles-Derived Slip Rates

Fault name	Model-predicted slip rate (mm/year)	GNSS velocity profile derived fault parallel slip rate (mm/year)	GNSS velocity profile-derived fault normal slip rate (mm/year)
Anninghe	4.5–5.0	5 ± 2	1 ± 1 (contraction)
Zemuhe	4.5–5.0	5 ± 1	1 ± 1 (extension)
Daliangshan (north)	4.5–5.0	5 ± 2	0~1 (contraction)
Daliangshan (middle)	4.5–5.0	4 ± 2	2 ± 2 (contraction)
Daliangshan (south)	4.5–5.0	5 ± 2	3 ± 2 (contraction)
Mabian (north)	1.5–2.0	2 ± 1	1 ± 1 (contraction)
Mabian (south)	1.5–2.0	0~1	2 ± 1 (contraction)

size decreases and tectonic faulting increases, the two end-member models converge. We thus propose that both the microplate and continuum deformation mechanisms are present in the southeastern margin of the Tibetan Plateau; the local tectonics is best explained by the microplate model, but scale of the kinematics makes its regional motion more consistent with the continuum model.

7. Conclusions

We calculate a GNSS velocity field using 142 GNSS sites spanning the 1999–2018 time interval, with more than 40 sites deployed within the central XXFS, to provide a new secular velocity solution for the southeastern margin of the Tibetan Plateau and Sichuan Basin that is made available through the UNAVCO repository and as a supplement. With this data, we employ an Euler pole clustering algorithm and *F* tests to revise the kinematics of this region. We confirm that the ADS is a distinct, rigid block, and we resolve a new, rigid DYB to the east bounded by the Yingjing-Mabian fault. Kinematic modeling predicts long-term slip rates that suggest both the ADS and the DYB partition (~10.0–12.0 mm/year) relative motion between the Tibetan Plateau and south China block in the central XXFS, reconciling with geological observations. We suggest that both the continuum and the microplate deformation patterns are present in the southeastern margin of the Tibetan Plateau, of which the local tectonics is better explained by the microplate model, but scale of the kinematics makes its broader-scale motion more consistent with the continuum model.

Acknowledgments

We thank Associate editor Yosuke Aoki and two anonymous reviewers for their thorough and constructive reviews, which greatly improved the quality of this manuscript. We thank the Crustal Movement Observation Network of China for providing access (<http://neiscn.org/>) to their data for publication in this manuscript. The raw position time series of GNSS sites are available at <https://zenodo.org/record/3266874#.XRx1D9UzbX4>. The derived GNSS velocity solution can be found in the supporting information (Data Set S1) and the UNAVCO repository (<https://www.unavco.org>). Rui Xu was funded by NSF of China: 41704014 and 41631073 and by the science and technology innovation fund of Sichuan Earthquake Agency (201804).

References

- Allen, C. R., Zhuoli, L., Hong, Q., Xueze, W., Huawei, Z., & Weishi, H. (1991). Field study of a highly active fault zone: The Xianshuihe fault of southwestern China. *Geological Society of America Bulletin*, 103(9), 1178–1199. [https://doi.org/10.1130/0016-7606\(1991\)103<1178:FSOAH>2.3.CO;2](https://doi.org/10.1130/0016-7606(1991)103<1178:FSOAH>2.3.CO;2)
- Altamimi, Z., Métivier, L., & Collilieux, X. (2012). ITRF2008 plate motion model. *Journal of Geophysical Research*, 117, B07402. <https://doi.org/10.1029/211JB008930>
- Bürgmann, R. (2000). Earthquake potential along the northern Hayward fault, California. *Science*, 289(5482), 1178–1182. <https://doi.org/10.1126/science.289.5482.1178>
- Chaussard, E., Bürgmann, R., Fattah, H., Nadeau, R. M., Taira, T., Johnson, C. W., & Johanson, I. (2015). Potential for larger earthquakes in the East San Francisco Bay Area due to the direct connection between the Hayward and Calaveras Faults. *Geophysical Research Letters*, 42, 2734–2741. <https://doi.org/10.1002/2015GL063575>
- Chen, Z. H., Burchfiel, B. C., Liu, Y., King, R. W., Royden, L. H., Tang, W., et al. (2000). Global Positioning System measurements from eastern Tibet and their implications for India/Eurasia intercontinental deformation. *Journal of Geophysical Research*, 105(B7), 16,215–16,227. <https://doi.org/10.1029/2000JB900092>
- Cheng, J., Liu, J., Gan, W. J., Yu, H. Z., & Li, G. (2011). Characteristics of strong earthquake evolution around the eastern boundary faults of the Sichuan-Yunnan rhombic block. *Science China Earth Science*, 54(11), 1716–1729. <https://doi.org/10.1007/s11430-011-4290-2>
- Cheng, J., Liu, J., Xu, X. W., & Gan, W. J. (2014). Tectonic characteristics of strong earthquakes in Daliangshan sub-block and implications of the Ms6.5 Ludian earthquake in 2014 on the surrounding faults (in Chinese). *Seismology and geology*, 36(4), 1228–1243.
- Copley, A., & McKenzie, D. (2007). Models of crustal flow in the India-Asia collision zone. *Geophysical Journal International*, 169(2), 683–698. <https://doi.org/10.1111/j.1365-246X.2007.03343.x>
- Deng, Q., Zhang, P., & Ran, Y. (2003). Basic characteristics of active tectonics of China. *Science in China Series D*, 46, 356–372.
- Densmore, A. L., Ellis, M. A., Li, Y., Zhou, R., Hancock, G. S., & Richardson, N. (2007). Active tectonics of the Beichuan and Pengguan faults at the eastern margin of the Tibetan Plateau. *Tectonics*, 26, TC4005. <https://doi.org/10.1029/2006TC001987>
- Dong, D. N., Herring, T. A., & King, R. W. (1998). Estimating regional deformation from a combination of space and terrestrial geodetic data. *Journal of Geodesy*, 72(4), 200–214. <https://doi.org/10.1007/s001900050161>
- Du, P. S. (1994). Study on paleoseismic activity characteristics since late Quaternary and paleoearthquakes of Zemuhe Fault (in Chinese). *Earthquake Research Sichuan*, 1, 42–52.
- Du, P. S. (2000). Slip displacement and its rate about Zemuhe Fault (in Chinese). *Earthquake Research Sichuan*, 1–2, 49–64.
- England, P., & Houseman, G. (1986). Finite strain calculations of continental deformation: 2. Comparison with the India-Asia collision zone. *Journal of Geophysical Research*, 91(B3), 3664–3676. <https://doi.org/10.1029/JB091iB03p03664>

- Gordon, R. G., Stein, S., DeMets, C., & Argus, D. F. (1987). Statistical tests for closure of plate motion circuits. *Geophysical Research Letters*, 14(6), 587–590. <https://doi.org/10.1029/GL014i006p00587>
- Guzman-Speziale, M. (1996). *Seismicity and active tectonics of the western Sunda Arc. The tectonic evolution of Asia* (pp. 63–84). Cambridge University Press.
- Han, W. B., & Jiang, G. F. (2004). Study on distribution characteristics of strong earthquakes in Sichuan-Yunnan area and their geological tectonic background. *Acta Seismologica Sinica*, 17(2), 230–243.
- Harrison, T. M., Copeland, P., Kidd, W. S. F., & Yin, A. N. (1992). Raising tibet. *Science*, 255(5052), 1663–1670.
- He, H., Ikeda, Y., He, Y., Togo, M., Chen, J., Chen, C. Y., et al. (2008). Newly-generated Daliangshan Fault Zone—Shortcutting on the central section of Xianshuihe-Xiaojiang fault system. *Science in China Series D: Earth Sciences*, 51(9), 1248–1258. <https://doi.org/10.1007/s11430-008-0094-4>
- He, H. L., Ran, H. L., & Yasutaka, I. (2006). Uniform strike-slip rate along the Xianshuihe-Xiaojiang fault system and its implications for active tectonics in southeastern Tibet. *Acta Geologica Sinica*, 80(3), 376–386. <https://doi.org/10.1111/j.1755-6724.2006.tb00255.x>
- He, H. L., Song, F. M., & Li, C. Y. (1999). Topographic survey of micro faulted landform and estimation of strike slip rate for the Zemuhe Fault, Sichuan Province. *Seismology and Geology*, 21(4), 361–369.
- He, H. L., Yasutaka, I., Song, F. M., & Dong, X. Q. (2002). Late quaternary slip rate of the Xiaojiang fault and its implication. *Seismology and Geology*, 24(1), 14–26.
- He, H. L., & Yasutakyr, I. (2007). Faulting on the Anninghe Fault zone, southwest China in late Quaternary and its movement model. *Acta Seismologica Sinica*, 29(5), 537–548.
- He, J., & Lu, S. (2007). Lower friction of the Xianshuihe-Xiaojiang fault system and its effect on active deformation around the southeastern Tibetan margin. *Terra Nova*, 19(3), 204–210. <https://doi.org/10.1111/j.1365-3121.2007.00735.x>
- Herring, T. A. (2003). GLOBK: Global Kalman filter VLBI and GPS analysis program version 10.1, Internal memorandum, Massachusetts Institute of Technology, Cambridge.
- Herring, T. A., King, R. W., Floyd, M. A., & McClusky, S. C. (2016). Introduction to GAMIT/GLOBK, Release 10.6, Massachusetts Institute of Technology. http://geoweb.mit.edu/~simon/gtgt/Intro_GG.pdf
- Herring, T. A., King, R. W., & McClusky, S. C. (2010). Documentation of the MIT GPS Analysis Software: GAMIT Release 10.4, Massachusetts Institute of Technology, Cambridge.
- Houseman, G., & McKenzie, D. P. (1982). Numerical experiments on the onset of convective instability in the Earth's mantle. *Geophysical Journal of the Royal Astronomical Society*, 68(1), 133–164. <https://doi.org/10.1111/j.1365-246X.1982.tb06966.x>
- Jiang, G., Xu, X., Chen, G., Liu, Y., Fukahata, Y., Wang, H., et al. (2015). Geodetic imaging of potential seismogenic asperities on the Xianshuihe-Anninghe-Zemuhe fault system, southwest China, with a new 3-D viscoelastic interseismic coupling model. *Journal of Geophysical Research: Solid Earth*, 120, 1855–1873. <https://doi.org/10.1002/2014JB011492>
- Jun, S., Yipeng, W., & Fangmin, S. (2003). Characteristics of the active Xiaojiang fault zone in Yunnan, China: A slip boundary for the southeastward escaping Sichuan-Yunnan Block of the Tibetan Plateau. *Journal of Asian Earth Sciences*, 21(10), 1085–1096. [https://doi.org/10.1016/S1367-9120\(02\)00185-2](https://doi.org/10.1016/S1367-9120(02)00185-2)
- King, R. W., Shen, F., Clark Burchfiel, B., Royden, L. H., Wang, E., Chen, Z., et al. (1997). Geodetic measurement of crustal motion in southwest China. *Geology*, 25(2), 179. [https://doi.org/10.1130/0091-7613\(1997\)025<0179:GMOCMI>2.3.CO;2](https://doi.org/10.1130/0091-7613(1997)025<0179:GMOCMI>2.3.CO;2)
- Kreemer, C., Blewitt, G., & Klein, E. C. (2014). A geodetic plate motion and global strain rate model. *Geochemistry, Geophysics, Geosystems*, 15, 3849–3889. <https://doi.org/10.1002/2014GC005407>
- Kuwahara, Y., Kiguchi, T., Lei, X., Ma, S., Wen, X., & Chen, S. (2012). Stress state along the Anninghe-Zemuhe fault zone, southwestern China, estimated from an array of stress orientation measurements with a new method. *Earth, Planets and Space*, 64(1), 13–25. <https://doi.org/10.5047/eps.2011.08.017>
- Leloup, P. H., Lacassin, R., Tappognier, P., Schärer, U., Zhong, D., Liu, X., et al. (1995). The Ailao Shan-Red River shear zone (Yunnan, China). Tertiary transform boundary of Indochina. *Tectonophysics*, 251(1–4), 3–84. [https://doi.org/10.1016/0040-1951\(95\)00070-4](https://doi.org/10.1016/0040-1951(95)00070-4)
- Loveless, J. P., & Meade, B. J. (2011). Partitioning of localized and diffuse deformation in the Tibetan Plateau from joint inversions of geologic and geodetic observations. *Earth and Planetary Science Letters*, 303(1–2), 11–24. <https://doi.org/10.1016/j.epsl.2010.12.014>
- Lyons, S. N., Bock, Y., & Sandwell, D. T. (2002). Creep along the Imperial Fault, southern California, from GPS measurements. *Journal of Geophysical Research*, 107(B10), 2249. <https://doi.org/10.1029/2001JB000763>
- McCaffrey, R. (2005). Block kinematics of the Pacific-North America plate boundary in the southwestern US from inversion of GPS, seismological, and geologic data. *Journal of Geophysical Research*, 110, B07401. <https://doi.org/10.1029/2004JB003307>
- McCaffrey, R., Qamar, A. I., King, R. W., Wells, R., Khazaradze, G., Williams, C. A., et al. (2007). Fault locking, block rotation and crustal deformation in the Pacific Northwest. *Geophysical Journal International*, 169(3), 1315–1340. <https://doi.org/10.1111/j.1365-246X.2007.03371.x>
- McClusky, S., Balassanian, S., Barka, A., Demir, C., Ergintav, S., Georgiev, I., et al. (2000). Global Positioning System constraints on plate kinematics and dynamics in the eastern Mediterranean and Caucasus. *Journal of Geophysical Research*, 105(B3), 5695–5719. <https://doi.org/10.1029/1999JB900351>
- Meade, B. J. (2007). Present-day kinematics at the India-Asia collision zone. *Geology*, 35(1), 81–84. <https://doi.org/10.1130/G22924A.1>
- Qian, H. (1992). The new active fault on the north segment of the Anninghe fault and its potential seismic capability research (in Chinese). *Seismology and Geology*, 14.
- Qian, H., Luo, Z. L., & Wen, X. Z. (1990). Preliminary study of characteristic earthquakes in the Xianshui fault zone (in Chinese). *Acta Seismologica Sinica*, 12(1), 22–29.
- Qiao, X. J., Wang, Q., & Du, R. L. (2004). Characteristics of current crustal deformation of active blocks in the Sichuan-Yunnan region (in Chinese). *Chinese Journal of Geophysics*, 47(5), 805–811.
- Ran, Y. H., Cheng, J. W., Gong, H. L., & Chen, L. C. (2008). Late quaternary geomorphic deformation and displacement rates of the Anninghe Fault around Zimakua. *Seismology and Geology*, 30(1), 86–98.
- Reilinger, R., McClusky, S., Vernant, P., Lawrence, S., Ergintav, S., Cakmak, R., et al. (2006). GPS constraints on continental deformation in the Africa-Arabia-Eurasia continental collision zone and implications for the dynamics of plate interactions. *Journal of Geophysical Research*, 111, B05411. <https://doi.org/10.1029/2005JB004051>
- Replumaz, A., & Tapponnier, P. (2003). Reconstruction of the deformed collision zone between India and Asia by backward motion of lithospheric blocks. *Journal of Geophysical Research*, 108(B6), 2285. <https://doi.org/10.1029/2001JB000661>
- Royden, L. H., Burchfiel, B. C., King, R. W., Wang, E., Chen, Z., Shen, F., & Liu, Y. (1997). Surface deformation and lower crustal flow in eastern Tibet. *Science*, 276(5313), 788–790. <https://doi.org/10.1126/science.276.5313.788>

- Royden, L. H., Burchfiel, B. C., & van der Hilst, R. D. (2008). The geological evolution of the Tibetan Plateau. *Science*, 321(5892), 1054–1058.
- Rui, X., & Stamps, D. S. (2016). Present-day kinematics of the eastern Tibetan Plateau and Sichuan Basin: Implications for lower crustal rheology. *Journal of Geophysical Research: Solid Earth*, 121, 3846–3866. <https://doi.org/10.1002/2016JB012839>
- Savage, J. C. (2018). Euler-vector clustering of GPS velocities defines microplate geometry in southwest Japan. *Journal of Geophysical Research: Solid Earth*, 123, 1954–1968. <https://doi.org/10.1002/2017JB014874>
- Savage, J. C., & Simpson, R. W. (2013). Clustering of GPS velocities in the Mojave block, southeastern California. *Journal of Geophysical Research: Solid Earth*, 118, 1747–1759. <https://doi.org/10.1002/2012JB009699>
- Shen, F., Royden, L. H., & Burchfiel, B. C. (2001). Large-scale crustal deformation of the Tibetan Plateau. *Journal of Geophysical Research*, 106(B4), 6793–6816. <https://doi.org/10.1029/2000JB900389>
- Shen, Z.-K., Lu, J., Wang, M., & Burgmann, R. (2005). Contemporary crustal deformation around the southeast borderland of the Tibetan Plateau. *Journal of Geophysical Research*, 110, B11409. <https://doi.org/10.1029/2004JB003421>
- Song F. M., Li, R. C., & Xu, X. W. (2002). Preliminary results of the investigation of Paleo-earthquakes along the Daliangshan fault zone, Sichuan province, China, Seismology and Geology.
- Stein, S., & Gordon, R. G. (1984). Statistical tests of additional plate boundaries from plate motion inversions. *Earth and Planetary Science Letters*, 69(2), 401–412. [https://doi.org/10.1016/0012-821X\(84\)90198-5](https://doi.org/10.1016/0012-821X(84)90198-5)
- Sternai, P., Avouac, J. P., Jolivet, L., Faccenna, C., Gerya, T., Becker, T. W., & Menant, A. (2016). On the influence of the asthenospheric flow on the tectonics and topography at a collision-subduction transition zones: Comparison with the eastern Tibetan margin. *Journal of Geodynamics*, 100, 184–197. <https://doi.org/10.1016/j.jog.2016.02.009>
- Sun, C. M., Wang, L., & Xie, W. (2010). *Compilation of Sichuan historical earthquakes (Volume 1, in Chinese)*. Sichuan: Peoples publish housing.
- Tang, R. C., & Han, W. B. (1993). *Active faults and earthquakes in Sichuan Province (in Chinese)*. Beijing: Seismological Press.
- Tapponnier, P., Peltzer, G., Le Dain, A. Y., Armijo, R., & Cobbold, P. (1982). Propagating extrusion tectonics in Asia: New insights from simple experiments with plasticine. *Geology*, 10(12), 611–616. [https://doi.org/10.1130/0091-7613\(1982\)10<611:PETIAN>2.0.CO;2](https://doi.org/10.1130/0091-7613(1982)10<611:PETIAN>2.0.CO;2)
- Thatcher, W. (2009). How the continents deform: The evidence from tectonic geodesy. *Annual Review of Earth and Planetary Sciences*, 37(1), 237–262. <https://doi.org/10.1146/annurev.earth.031208.100035>
- Thatcher, W. (2007). Microplate model for the present-day deformation of Tibet. *Journal of Geophysical Research*, 112, B01401.
- Wang, E. (1998). Late Cenozoic Xianshuuhe-Xiaojiang, Red River, and Dali fault systems of southwestern Sichuan and central Yunnan, China (Vol. 327). Geological Society of America.
- Wang, H., Liu, M., Cao, J., Shen, X., & Zhang, G. (2011). Slip rates and seismic moment deficits on major active faults in mainland China. *Journal of Geophysical Research*, 116, B02405. <https://doi.org/10.1029/2010JB007821>
- Wang, H., Ran, Y., Chen, L., & Li, Y. (2017b). Paleoearthquakes on the Anninghe and Zemuhe fault along the southeastern margin of the Tibetan Plateau and implications for fault rupture behavior at fault bends on strike-slip faults. *Tectonophysics*, 721, 167–178. <https://doi.org/10.1016/j.tecto.2017.08.030>
- Wang, W., Qiao, X., Yang, S., & Wang, D. (2017a). Present-day velocity field and block kinematics of Tibetan Plateau from GPS measurements. *Geophysical Journal International*, 208(2), 1088–1102. <https://doi.org/10.1093/gji/ggw445>
- Wang, Y. Z., Wang, E. N., Shen, Z. K., Wang, M., Gan, W. J., Qiao, X. J., et al. (2008). GPS-constrained inversion of present-day slip rates along major faults of the Sichuan-Yunnan region, China. *Science in China Series D-Earth Sciences*, 51(9), 1267–1283. <https://doi.org/10.1007/s11430-008-0106-4>
- Wen, X., Fan, J., Yi, G., Deng, Y., & Jong, F. (2008). A seismic gap on the Anninghe fault in western Sichuan, China. *Science in China Series D-Earth Sciences*, 51(10), 1375–1387. <https://doi.org/10.1007/s11430-008-0114-4>
- Wen, X. Z. (1993). Rupture segmentation and assessment of probabilities of seismic potential on the Xiaojiang fault zone. *Acta Seismologica Sinica*, 6(4), 993–1004. <https://doi.org/10.1007/BF02651834>
- Wen, X. Z., Du, F., & Yi, G. X. (2013). Earthquake potential of the Zhaotong and Lianfeng fault zones of the eastern Sichuan-Yunan border region (in Chinese). *Chinese Journal of Geophysics*, 56(10), 3361–3372. <https://doi.org/10.6038/cjg20131012>
- Xiang, H. F., Xu, X. W., Guo, S. M., Zhang, W. X., Li, H. W., & Yu, G. H. (2002). Sinistral thrusting along the Lijiang-Xiaojinhe fault since the quaternary and its geologic-tectonic significance - Shielding effect of transverse structure of intracontinental active block. *Seismology and Geology*, 24(2).
- Xu, X., Wen, X., Zheng, R., Ma, W., Song, F., & Yu, G. (2003). Pattern of latest tectonic motion and dynamics of faulted blocks in Yunnan and Sichuan (in Chinese). *Science in China Series D-Earth Sciences*, 33, 151–162.
- Xu, X. W., Jiang, G. Y., & Yu, G. H. (2014). Discussion on seismogenic fault of the Ludian Ms 6.5 earthquake and its tectonic attribution (in Chinse). *Chinese Journal of Geophysics*, 57(9), 3060–3068.
- Xu, Z., Huang, Z., Wang, L., Xu, M., Ding, Z., Wang, P., et al. (2016). Crustal stress field in Yunnan: Implication for crust-mantle coupling. *Earthquake Science*, 29(2), 105–115. <https://doi.org/10.1007/s11589-016-0146-3>
- Yi, G. X., Wen, X. Z., Zhang, Z. W., Long, F., Ruan, X., & Du, F. (2010). Study on potential strong earthquake risk in Mabian Area, Southern Sichuan. *Seismology and Geology*, 32(2). <https://doi.org/10.3969/j.issn.0253-4967.2010.02.011>
- Zhang, P., Deng, Q., Zhang, G., Ma, J., Gan, W., Min, W., et al. (2003). Active tectonic blocks and strong earthquakes in the continent of China. *Science in China Series D: Earth Sciences*, 46(2), 13–24.
- Zhang, P. Z. (2013). A review on active tectonics and deep crustal processes of the Western Sichuan region, eastern margin of the Tibetan Plateau. *Tectonophysics*, 584, 7–22. <https://doi.org/10.1016/j.tecto.2012.02.021>
- Zhang, P.-Z. (2012). A review on active tectonics and deep crustal processes of the Western Sichuan region, eastern margin of the Tibetan Plateau. *Tectonophysics*, 584, 7–22.
- Zhang, S. M., Nie, G. Z., Liu, X. D., Ren, J. J., & Su, G. (2005). Kinematical and structural patterns of Yingjing-Mabian-Yanjin thrust fault zone, southeast of Tibetan Plateau, and its segmentation from earthquakes. *Seismology and Geology*, 27(2), 221–233.
- Zhang, S. M., & Xie, F. R. (2001). Seismo-tectonic divisions of strong earthquakes ($M_s \geq 7.0$) and their tectonic geomorphology along Xianshuuhe-Xiaojiang fault zone. *Acta Geologica Sinica*, 23(1), 36–44.
- Zhang, Z. Q., McCaffrey, R., & Zhang, P. (2013). Relative motion across the eastern Tibetan Plateau: Contributions from faulting, internal strain and rotation rates. *Tectonophysics*, 584, 240–256. <https://doi.org/10.1016/j.tecto.2012.08.006>
- Zhao, J., Zai-Sen, J., An-Fu, N., Jie, L., Yan-Qiang, W., Wen-Xin, W., et al. (2015). Study on dynamic characteristics of fault locking and fault slip deficit in the eastern boundary of the Sichuan-Yunan rhombic block (in Chinese). *Chinese Journal of Geophysics*, 58(3), 872–885. <https://doi.org/10.6038/cjg20150316>

- Zheng, G., Wang, H., Wright, T. J., Lou, Y., Zhang, R., Zhang, W., et al. (2017). Crustal deformation in the India-Eurasia collision zone from 25 years of GPS measurements. *Journal of Geophysical Research: Solid Earth*, 122, 9290–9312. <https://doi.org/10.1002/2017JB014465>
- Zhou, R. J., Li, X. G., Huang, Z. Z., He, Y. L., & Ge, T. R. (2003). Average slip rate of Daliang Mountain fault zone in Sichuan in Late Quaternary Period (in Chinese). *Journal of Seismological Research*, 26(2), 191–196.

References From the Supporting Information

- Cui, Z. J., Chen, Z. L., Wang, Q. C., & Li, J. (2019). Characteristics of focal mechanism and stress in the North-South seismic belt of China (in Chinese). *Earthquake*, 39(1), 1–10.